Upgrading Traditional Poly(1,3-dioxolane) Electrolytes via Integrated Design of Ultra-Stable Network for Solid-State Lithium Metal Batteries

Hao Li
Henan University
YunFei Du
https://orcid.org/0000-0002-9439-0235
Long Zhao
Henan University
Chenyu Xiong
University of Science and Technology Beijing
Erqing Zhao
Henan Institute of Science and Technology
Changgong Li
Henan Institute of Science and Technology
Shumeng Hao
Beijing University of Chemical Technology
Weidong Zhou (zhouwd@mail.buct.edu.cn)
Beijing University of Chemical Technology

Article

Keywords: solid state batteries, poly(1,3-dioxolane), network, solid electrolytes

Posted Date: September 19th, 2022

DOI: https://doi.org/10.21203/rs.3.rs-2003311/v1

Abstract

Poly(1,3-dioxolane) (PDOL)-based solid electrolytes are expected to be exploited in solid-state lithium metal batteries (SLMBs) due to their high ionic conductivity, good lithium metal compatibility, and facile preparation method of *in-situ* polymerization in cells. However, inferior structural stability and low Li-ion transference number (t_{Li+}) still impede PDOL from authentic commercialization. Herein we propose a novel ultrathin crosslinked PDOL-based electrolyte (PTADOL), which is prepared *via* a multifunctional trimethylolpropane tris[3-(2-methyl-1-aziridine) propionate] additive. The *in-situ* formed PTADOL not only affords an integrated network configuration with stabilized electrode/electrolyte interface, but also achieves improved oxidative stability, excellent thermal stability, and superior flame retardancy. Moreover, PTADOL has rational O-Li^+ coordination for fast Li^+ transport, which enhances both ionic conductivity and t_{Li+}. Based on the ultra-stable PTADOL, the high voltage $LiNi_{0.8}Mn_{0.1}Co_{0.1}O_2$||Li batteries exhibit excellent electrochemical performance without electrolyte degradation. This work provides a practical approach to designing a highly stable solid polymer electrolyte for high-performance SLMBs.

Introduction

Rechargeable lithium-ion batteries are the power source for most of today's electric vehicles, unmanned planes, and portable electronic devices.[1] So far, remaining drawbacks including the unsatisfactory energy and power density, poor safety and stability, and limited operational conditions restrict their future potentials.[2] Solid-state lithium metal batteries (SLMBs) consisting of Li^+ conducting solid-state electrolytes (SSEs) and metallic lithium anodes (3860 mAh g^{-1}) are considered a prospective approach to solving the above problems. However, it is also acknowledged that the practical application of SLMBs is seriously impeded by uncontrolled Li dendrites and inferior solid-solid interfacial stabilities.[3–6] Great efforts have been dedicated through many strategies to overcome these obstacles, among which exploring safe and stable SSEs with compatibility to electrodes is particularly critical and indispensable.

Solid polymer electrolytes (SPEs) have been demonstrated as potential candidates to improve energy density and alleviate the interfacial issue of SLMBs, as their lightweight, suitable interfacial wettability property, and manufacturing scalability enable them to construct a compact solid/solid interface and thus accommodate the volume change of the electrodes during battery operations.[7] SPEs with polar groups (e.g., ether, ester, nitrile, fluorine groups) realize Li^+ transportation through the coordination-dissociation interaction during the rotation and vibration of the polymer chains.[8, 9] Among all types of SPEs, poly(ethylene oxide) (PEO) based SPEs have been the most extensively studied system since 1973,[10] owing to its good lithium salt solubility, excellent film-forming property and acceptable anodic stability.[11] Nevertheless, large thermodynamic driving force for macromolecular stacking and crystallization in PEO-based SPEs generally yield low ambient-temperature ionic conductivity (~ 10^{-5} S cm^{-1}); and it is difficult to infiltrate the highly viscous molten PEO into the nano-sized pores of intercalating cathodes, especially when high-loading materials are utilized for enhanced energy density.[12, 13] Meanwhile, poly (1,3-dioxolane) (PDOL) based SPEs which are always fabricated by *in-situ*

polymerization of lowviscous 1,3-dioxolane (DOL) electrolytes inside a battery cell, are of particular interest because this polymer effectively reduces contact impedance of electrodes/electrolyte interfaces and forms chemically stable interphases on Li metal and thereby enables highly reversible cycling of the batteries.[14–16] Furthermore, the alternative copolymerization of C-C-O and C-O-C segments further reduced the crystallinity of polymer chains and thus improved the ionic conductivity of SPEs towards 10^{-4} S cm^{-1}. Whereas, the excessive ether-Li^+ coordination leads to large activation energy for cation motion and thus reduces Li-ion transference number (t_{Li+}) of these SPEs (usually 0.2 ~ 0.3).[8, 17] This leads to ionic concentration gradients and reversed electric field in the cell, which in turn results in large overpotentials, limited rate capacity, and exceptionally rapid dendrite growth.[18, 19] Meanwhile, the poor mechanical strength/stability of linear PDOL is insufficient to prevent itself from lithium dendrite penetration.[20, 21] In addition, the narrow electrochemical stability window (ESW) and flammability hazard also greatly limit their selectivity in high-voltage ternary cathodes.

To address the above issues, herein, we report a new strategy that uses trimethylolpropane tris[3-(2-methyl-1-aziridine) propionate] (TTMAP) as the functional crosslinker to form a new type of PDOL-based SPEs with ultra-stable network structure (marked as PTADOL). In addition to reacting with terminal hydroxyl to improve the oxidative stability of PTADOL, trident TTMAP with abundant carboxyl also effectively weakens the O-Li^+ coordination, realizing high t_{Li+} of 0.76 with no compromise of ionic conductivity of 1.38×10^{-4} S cm^{-1} (Fig. 1a). Moreover, the PTADOL featured nonflammable characteristics because of the superior thermal stability of the TTMAP additive, which improved the safety of SLMBs. Benefiting from the unique nanotopology structure and assistance of multifunctional TTMAP, the resultant PTADOL can expand ESW, boost ion conduction, enhance mechanical property, and improve thermal stability. As a result, the as-constructed Li symmetric cells exhibit ultralong cycling stability, and the high voltage $LiNi_{0.8}Mn_{0.1}Co_{0.1}O_2$||Li batteries show excellent electrochemical performance without electrolyte degradation. This study offers a facile and practical approach to designing highly stable SPEs for high-performance SLMBs.

Results And Discussion

Structural characterization of PTADOL. The liquid-state ^{13}C NMR spectra in Supplementary Fig. 1 reveal DOL has two characteristic peaks at 64.1 and 94.5 ppm corresponding to -O-CH_2-CH_2-O- and -O-CH_2-O- units. After the addition of 0.8 wt% tris(pentafluorophenyl)borane (TFB) as initiator and 1.5M lithium bis(trifluoromethanesulfonyl)imide (LiTFSI) and stayed for 24 h, the obtained PDOL sample in Fig. 1b exhibits two new peaks at 66.9 and 95.2 ppm, indicating successful polymerization of DOL molecules. And the residual DOL can be calculated to 10.11% from the integrated area of the PDOL spectra, implying an incomplete polymerization reaction. The PTADOL was prepared by mixing TTMAP, DOL, LiTFSI with TFB as the initiator (Supplementary Fig. 2,). It was found that the obtained PTADOL is insoluble in most of deuterated solvents even after stirring for 24 h, and no characteristic peak of PDOL or DOL was detected in liquid NMR spectra (Supplementary Fig. 3). These results demonstrate superior structural

stability of PTADOL, which is quite different from PDOL SPE (Supplementary Fig. 4). The solid-state NMR characterization was used to reveal the crosslinked polymerization of the PTADOL electrolyte. As shown in Fig. 1d, chemical resonance shifts from 171.0 ppm (Fig. 1c) to 176.6 ppm corresponded to C = O from the TTMAP groups. And the downfield displacement of chemical shifts indicates the weakened shielding effect on the electronic environment of ^{13}C nuclei, which contributes to the redistribution of the electron density of the carbonyl groups.[22, 23] Furthermore, chemical shifts at 70.5 and 76.2 ppm in the PTADOL sample are assigned to short ether chains compare to that of pure TTMAP. The tremendous change in the chemical environment of oxygen atoms implies the alterant O-Li^+ coordination, which affects Li^+ transportation in PTADOL.

Furthermore, Fourier transform infrared spectroscopy (FTIR) measurement was conducted to verify the structure of PTADOL (Supplementary Fig. 5). Compared to PDOL, the absence of -OH peak in PTADOL indicates that the terminal hydroxyl of ether chains was end-capped by highly reactive aziridine from TTMAP *via* copolymerization. Besides, the X-ray diffraction (XRD) result (Supplementary Fig. 6) shows broad diffusion peaks between 10° and 35° in PTADOL, indicating the amorphous state and complete dissolution of LiTFSI.

Structure-dependent ion transport properties. The temperature-dependent ionic conductivity of the electrolytes was demonstrated in Fig. 2a. As is well known that the ionic conductance of SPEs with network structure is always inferior to that of the polymers with linear configuration due to the limited motion of conductive segments in crosslink structure. However, interestingly, the ionic conductivity of PTADOL at room temperature is 1.48×10^{-4} S cm^{-1}, which is even slightly larger than that of the PDOL sample (1.29×10^{-4} S cm^{-1}). And the curve for PTADOL appears less steep than that of PDOL, suggesting lower activation energy for ion motion (Supplementary Table 1).[24] To study the Li^+ transportation in PTADOL electrolyte, FTIR spectroscopy was carried out in the range of 725 – 760 and 800 – 1400 cm^{-1}. As shown in Fig. 2b, the peaks at 741.2 and 746.8 cm^{-1} correspond to the free ions and ion-pairs, respectively, which represents the intensity of the interaction between Li^+ and $TFSI^-$.[25, 26] Obviously, PTADOL has a larger ratio of free Li^+ than that of PDOL, indicative of higher carrier concentration in the polymer system. Figure 2c shows that the characteristic peak of the long-chained PDOL at 845 cm^{-1} cannot be observed in PTADOL sample, demonstrating the alternative copolymerization of DOL and TTMAP. And the enhanced C-H out-of-plane peaks at 915 cm^{-1} indicate a spatial polymeric structure formed in PTADOL. In addition, for PDOL sample, vibrational peaks at about 1000 cm^{-1} are assigned to the C-O-C stretching; these peaks dramatically shift to 1060 cm^{-1} in PATDOL, suggesting a great change of O-Li^+ interaction in the network structure. Moreover, the electrostatic potential calculated by Density Functional Theory (DFT) in Supplementary Fig. 7–8 demonstrates that the red areas in ester group from TTMAP and ether group from PDOL represent uniform negative electrostatic potential, which induces the interaction with Li^+ and contributes to high solubility and good dissociation of lithium salts in PTADOL.

For a better understanding of the ion transfer dynamics and molecule structure, Molecular Dynamics (MD) simulations were performed to elucidate the subtle interactions of Li^+ ions with the polymer host in PTADOL and PDOL electrolytes. The atomic position and the trajectory of the ions were convoluted because of the thermal effect; therefore, deconvolution of the ionic trajectories was necessary to show clearly the ion interactions. Figure 2d-g show the snapshots of the simulated PTADOL and PDOL electrolytes, respectively. The snapshots of the local coordination structure in Fig. 2f demonstrate that Li^+ tends to coordinate with four oxygen atoms from the ether group in PTADOL. By contrast, five oxygen atoms from the ether group coordinate with one Li^+ in PDOL (Fig. 2g). Corresponding average bond distances of O-Li^+ bond in PTADOL (2.223 Å) are longer than that of PDOL (2.207 Å), suggesting that PTADOL coordinates less strongly to Li^+ than PDOL does (Supplementary Table 2). The introduction of trident TTMAP crosslinker with ester group weakened the O-Li^+ coordination in PTADOL compared to that of the PDOL sample, and the weaker interaction strength of nearby Li^+ is beneficial to enhancing the local diffusion of Li^+ along the polymer segments.[27] To further investigate the local coordination structural properties of SPE interacting with Li^+, the radial distribution functions (g(r), solid lines) and coordination numbers (CN, dash lines) of O-Li^+ were calculated. The g(r) plots in Fig. 2h and 2i display the dominated peaks at 2.1 Å for O-Li^+ ($TFSI^-$ and polymer chain) in both SPE systems, and the first Li^+ solvation sheath (≈ 3 Å) is primarily composed of the oxygen atom from ether groups and $TFSI^-$ anions, which implies the oxygen atom is the major type to coordinate with cation (Supplementary Fig. 9). And the g(r) of PTADOL shows a sharper peak, demonstrating a well-defined coordination sphere for Li^+ in the SPE system.[28] Besides, all peaks vanish at longer distances, indicating only very local ordering in this system. Furthermore, it can be seen directly from the CN of O-Li^+ in the first solvation sheath (Fig. 2i) that the CN in PDOL is significantly higher than that in PTADOL, which indicates a much stronger polymer-Li^+ coordination effect in PDOL. In contrast, stereoscopic PTADOL coordinates to Li^+ more weakly, allowing for a higher fraction of the applied potential to lead to cation transport.

Electrochemical characterization and intrinsic property of PTADOL. As mentioned above, rational O-Li^+ coordination results in the Li^+ ions being less immobilized and therefore facilitates faster lithium transport, which will favor an increase of t_{Li+} in SPEs.[2, 17] Accordingly, the t_{Li+} of PTADOL and PDOL were measured by chronoamperometry using Li||SPE||Li symmetric cell, and the chronoamperometry curves and the AC impedances before and after polarization of the cells are shown in Fig. 3a and Supplementary Fig. 10. There is a significant augment in t_{Li+} from 0.24 of PDOL to 0.76 of PTADOL (Supplementary Table 3), which is comparable to that of single-ion conductors (≥ 0.8). Moreover, from the DFT calculation (Supplementary Fig. 11), the adsorption energy for $TFSI^-$ of TTMAP group in PTADOL was −0.556 eV, which is favorable to the immobilization of anions and further improves the t_{Li+} of PTADOL. As shown in Fig. 3b, the ESW of the PTADOL can be stabilized up to 4.6 V with a standard leakage current of 20 μA, which is much higher than that of PDOL (4.0 V). It has been theoretically and experimentally confirmed that the terminal hydroxyl of ion-conductive polymers will be firstly oxidized at higher voltage, which is the main factor that limits the improvement of the ESW.[29, 30] Compared to PDOL, the aziridine

groups in TTAMP could react with terminal hydroxyl groups and reduce the chain length of polyether groups, which significantly improved the oxidation stability of PTADOL.[31]

The formation of 3D crosslinked amorphous polymer networks enables PTADOL to possess superior film-forming capability, transparent appearance, high mechanical flexibility, and excellent thermal stability. As shown in Supplementary Fig. 12–13, an ultrathin and flexible PTADOL film (~ 7.2 μm) has been fabricated by incorporating with polyethylene (PE) separator. The tensile strength of the as-prepared solid electrolytes was assessed by stress-strain curves (Fig. 3c). The elastic limit of PDOL electrolyte reaches 9.5 MPa, similar to that of pure PE separator (8.8 MPa). While for PTADOL sample, significant improvement of elastic limit (19.4 MPa) reveals that three-dimension crosslink structure of PTADOL could better resist elastic deformation under the influence of the external environment.

The thermal stability of SPEs directly determines the battery safety. Figure 3d shows the thermal gravity analysis (TGA) thermograms of polymer electrolytes. TGA curve of PDOL electrolyte show a sharp weight loss started at 107°C, indicating disaggregation of PDOL chains (Supplementary Fig. 14). Since the decomposition temperature of pure PDOL is about 300°C, incorporation of LiTFSI greatly reduce the thermal stability of PDOL electrolyte.[32] This can be attributed to electropositive carbon atom between the two electronegative oxygen atoms was vulnerable to be attacked by $TFSI^-$ anions at elevated temperature.[33] In contrast, PTADOL suffer no obvious weight drop until 400°C due to significant decline of terminal hydroxyl of polymer chains, demonstrating superior thermal stability of the network structure. To further simulate the thermal performance of the polymer electrolytes, the PTADOL and PDOL samples were sealed in glass fiber substrate, and then were put into an oven at 120°C for 20 mins. As seen in Fig. 3e and 3f, the PDOL sample quickly melted into liquid, while PTADOL maintained the original state. Furthermore, even at room temperature, PDOL slowly turned from solid into translucent liquid in 5 days and could not become solid again at room temperature (Supplementary Fig. 15), indicating an irreversible depolymerization of PDOL sample.[32] All these features indicate that the PTADOL is much more thermally stable than that of PDOL, emphasizing the importance of the network structure induced by TTMAP.

Characterization of the Li/PTADOL interface. Li symmetrical cells were assembled with PTADOL and PDOL to investigate the compatibility with lithium metal anode. Figure 4a displays interfacial impedance versus storage time of PTADOL based Li symmetric batteries. It is worth noting that the cells exhibit no obvious increase for bulk/interfacial resistances during 10 days of storage time, indicating superior chemical stability of the PTADOL/Li interface in the batteries. To evaluate the critical current density (CCD) of the PTADOL, rate performance test with a Li/Li symmetric cell was performed at current densities ranging from 0.1 to 2.6 mA cm^{-2} for 1 h per half cycle, the results of which are given in Fig. 4b. The PTADOL based battery shows an extremely high CCD in excess of 2 mA cm^{-2}, which can ascribe to the improvement of mechanical strength and t_{Li+} of the electrolyte. The long-term electrochemical compatibility of PTADOL with lithium metal was characterized by galvanostatic charging and discharging for 1 h at 0.25 mA cm^{-2} in Li symmetric cells. The cycling curves in Fig. 4c of PTADOL cell

show small overpotential of 20 mV, and excellent long-term stability for over 1300 h, which reveals a stable interface during the stripping/plating process. By contrast, PDOL battery suffered sharp overpotential augment after 700 h, and the heavy fluctuation of voltage hysteresis from insert graph implies uncontrolled growth of dendrites and continuous side reactions of Li at the anode/electrolyte interface.[34]

Moreover, high-resolution X-ray photoelectron spectroscopy (XPS) was conducted to characterize the composition and structure of SEI on cycled lithium metal in these two electrolytes and study the SPE/Li interfacial compatibility. The deconvolution of C 1s spectra in Fig. 4d reveals five peaks in PTADOL sample, representing C-C (284.8 eV), C-O (286.3 eV), O-C-O (288.8 eV), COOR (289.7 eV), and -CF_3 (292.5 eV, from $TFSI^-$).[20] Even after 1000 h cycling, the peak intensities of C-O, C-O-C, and COOR in PTADOL are significantly lower than that of PDOL sample after 200 h cycling (Fig. 4e), indicating a suppressed polymer degradation in PTADOL compared to the ether groups decomposition in PDOL that generates abundant organic species in SEI.[35] Besides, with the extension of etching time, -CF_3 concentrations in F 1s spectra of these two samples sharply decrease from 0 to 180 s as the LiF increases.[36, 37] Not coincidentally, PTADOL sample exhibits less -CF_3 and LiF peak intensities than that of PDOL, demonstrating suppressed $TFSI^-$ anion diffusion and its decomposition accordingly in the network structure, which is in agreement with the obtained high t_{Li+} of PTADOL and the improved interfacial compatibility between PTADOL and lithium metal electrode.

Furthermore, morphology of lithium metal disassembled from cycled symmetric Li/Li batteries were characterized by scanning electron microscope (SEM). The surface of the lithium metal anode harvested from the PDOL is covered with Li dendrites, resulting in the deterioration of the interface stability (Fig. 4g). Corresponding cross-section SEM image in Supplementary Fig. 16 exhibits that the thickness of the rough and porous reaction layer of the lithium metal reached up to ~ 40 μm. When PTADOL was employed, effective suppression of Li dendrite growth was observed, and the lithium metal electrode demonstrates a much smoother surface (Fig. 4f). As shown in Supplementary Fig. 17, the surface of cycled lithium electrode harvested from the PTADOL maintained a metallic sheen, while anode from PDOL became darker after cycling. These results demonstrate that PTADOL with homogeneous and stable structure can construct efficient Li^+ transport channels in batteries, which effectively inhibit the accumulation of dendritic Li and suppress the expansion stress during the repeated process of stripping/plating.[38] Therefore, the intricate design of PTADOL is quite stable along with the continuous plating/stripping of lithium metal.

Battery Performance of PTADOL with Li anode and cathode. Rate performances of SLMBs with PTADOL and PDOL electrolytes were also tested at 30°C. The coin cells were made with $LiFePO_4$ (LFP) cathodes and lithium metal as anodes. By varying current densities from 0.1 to 2.0 C, LFP||PTADOL||Li cells deliver similar discharge capacities of 157, 150, 143, 137, 128, mAh g^{-1} compare to that of LFP||PDOL||Li cells (Fig. 5a and Supplementary Fig. 18). While with the current densities continue to increase, PTADOL cells exhibit much better discharge capacities of 119, and 110 mAh g^{-1} than PDOL samples (106, and 52 mAh

g^{-1}). The superior rate capacities can be attributed to the fast Li^+ conductance and the excellent interfacial compatibility due to the ultra-stable network structure of PTADOL electrolyte. It is also noteworthy that the PTADOL based battery shows extremely low overpotentials, i.e., 42, 59, 108 and 190 mV at 0.1, 0.2, 0.5, and 1 C, respectively (Fig. 5b). Moreover, overpotentials obtained from the discharge/charge profiles in Fig. 5c change almost-linearly with the discharge rate, which is typical for quasi single-ion conducting batteries.[39] Contrarily, the PDOL battery exhibits great overpotentials augment after 2 C. The differences in overpotentials are attributed to PTADOL battery with immobile anions only suffers from Ohmic overvoltage, while PDOL endure extra obvious concentration polarization at higher current density.[40] The LFP||PTADOL||Li cell exhibits superior cycling stability with 85.6% retention after 300 cycles at 2.5–4.0 V and 0.5 C (Supplementary Fig. 19); and it also shows very stable cycling for more than 200 cycles at 1 C, whereas the LFP||PDOL||Li cell decays dramatically within 100 cycles (Fig. 5d). Moreover, the typical voltage profiles of PTADOL based batteries (Fig. 5e) show negligible increased polarization voltages during long-term cycling than those of PDOL based batteries (Fig. 5f). The strong capability in suppressing Li dendrite growth, and fast Li^+ transport capability of PTADOL electrolyte enables us to explore battery performance with higher LFP loading. LFP||PTADOL||Li battery with 7.4 mg cm^{-2} loading enables reversible capacity of 154 mAh g^{-1} at 0.1 mA cm^{-2} and 146 mAh g^{-1} at 0.3 mA cm^{-2}, respectively (Fig. 5g). Furthermore, areal capacity of 3.34 mAh cm^{-2} was obtained when the LFP loading increased to 22.8 mg cm^{-2} at 0.1 mA cm^{-2} (Fig. 5h). More importantly, there is no obvious increase of overpotentials compared to those in the regular testing, and the typical charge/discharge plateaus are clearly identified (Supplementary Fig. 20), indicating great potential of PTADOL for application in high-performance SLMBs.

The expanded ESW of PTADOL make it compatible with high-voltage ternary cathodes. As indicated in Fig. 6a, the NMC811||PTADOL||Li cell displayed initial discharge capacity of 209.2 mAh g^{-1} at 0.1 C and 193.7 mAh g^{-1} at 0.5 C; And the capacity retention was still around 158.4 mAh g^{-1} after 150 cycles, which corresponds to a retention of 81.4% of the highest 0.5 C discharge capacity (194.5 mAh g^{-1}), indicating a stable electrochemical behavior of this PTADOL. Whereas, the NMC811||PDOL||Li cell suffered rapid capacity decay and failed after only 5 cycles. Supplementary Fig. 21 and Fig. 6b present the voltage profiles of the NMC811||PTADOL||Li cell at current density of 0.1 C and 0.5 C, respectively; the curves show clear potential plateaus without abnormal or unstable profiles even at 4.3 V cut-off voltage, demonstrating reversible and stable cycling processes.

Furthermore, operando differential electrochemical mass spectrometry (DEMS) was employed to explore the decomposition mechanism of SPEs using high-voltage cathode materials. A special designed battery mold consisting of NMC811||SPE||Li was set to charge and discharge at cutoff voltage of 4.3 V (Supplementary Fig. 22). As seen in Fig. 6c, no obvious gas generation was detected from PTADOL based battery throughout the whole cycles, demonstrating ultra-stable electrochemical stability of the network structure. In comparison, obvious O_2 release occurred during the first cycle of PDOL based battery (Fig. 6d), which can attribute to the decomposition of residual DOL molecules in the electrolyte. Gas generation reoccurred at ~ 4.2 V in the second cycle and continued through the third cycle. As

aforementioned, the terminal hydroxyl units in PDOL chain are generally more vulnerable than the units in the middle of molecular chain, which will initiate a chain reaction once the terminal units are decomposed.[41] These results show that the formed network topological structure in PTADOL greatly improve its oxidation stability with transition metal oxide cathode.

Safety assessment of solid-state pouch cells. NMC811||Li solid pouch cell with PTADOL was further fabricated to demonstrate the safety of the battery under various mechanical and thermal abuses. As shown in Supplementary Fig. 23 and Fig. 7a, the pouch cell works well after being folded without noticeable dimming. Subsequently, the cell underwent harsh nail penetration tests and then was cut into pieces. Impressively, the pouch cell can still be able to power the LED array without any flame or explosion (Fig. 7b-c). It is attributed to the excellent adhesive ability of PTADOL induced by TTMAP and the *in-situ* polymerization method, which is not easy to leak or volatilize, so after the pouch cell was cut, PTADOL maintained the reaction interface of the electrodes/SPE to ensure the normal operation of the cell. Additionally, the PTADOL-wrapped electrode can avoid being directly exposed to the air even after the cell fracture is split (Fig. 7d), thus retarding the side reactions between electrodes and the air and guaranteeing the regular operation of the cell. Furthermore, the flammability tests in Fig. 7e and Supplementary Video 1 show that the PDOL based battery burst into flame as soon as contacting with the fire. In sharp contrast, the PTADOL based battery did not burn even in repeat contact with the flame (Fig. 7f and Supplementary Video 2). The good flame retardancy comes from the superior thermal stability of TTMAP crosslinker, thus effectively preventing the cell burning.[42] Apparently, PTADOL has excellent thermal stability and the battery with PTADOL possess conformal and stable electrode/electrolyte interface.

In summary, a novel *in-situ* formed PTADOL SPE with ultra-stable network structure is well designed by introducing TTMAP as a multifunctional additive, which delivers high t_{Li+}, significantly expanded ESW, strong mechanical strength, and good flame retardancy. The PTADOL SPE improves the performance of SLMBs in four aspects. (1) Fast ion transportation. Benefited from unique structure of TTMAP, an integrated and stable three-dimensional network with rational O-Li^+ coordination forms after the *in-situ* polymerization, which guarantees abundant movable lithium ions and restricts the anions transportation. (2) Superior compatibility with lithium metal anode. The high mechanical stability induced by the stable network structure and high t_{Li+} enables uniform Li plating/striping without concentration polarization. (3) A significant expanded ESW. The oxidative stability of PTADOL has increased from 4.0 V to 4.6 V because of the stable network structure and the elimination of terminal hydroxyl, which makes it suitable to match with high-voltage cathodes. And applications of the PTADOL in NMC811||Li and LFP||Li batteries all display excellent electrochemical performances without electrolyte decomposition. (4) Outstanding thermal stability. The formed network structure protects PTADOL from depolymerization caused by $TFSI^-$; and the thermostable TTMAP further improves the flame retardancy of the batteries. This work provides new insights into the design of the advanced SPE system for high performance SLMBs.

Methods

Synthetic procedures of PTADOL. The precursor solvent for PTADOL was prepared by dissolving 1.5M bis(trifluoromethylsulfonyl)imide (LiTFSI, J&K) in 0.82 g 1,3-dioxolane (DOL, Aladdin) and 0.18 g trimethylolpropane tris[3-(2-methyl-1-aziridine) propionate] (TTMAP, Aladdin) mixture in an argon-filled glove box (H_2O < 0.1 ppm, O_2 < 0.1 ppm) at room temperature. Then 8 mg tris(pentafluorophenyl)borane (TFB, Aladdin) was added to the precursor solution, and stirred until completely dissolved. The prepared solution was soaked into polyethylene separator (~ 6 μm thick, Asahi) and it spontaneously converted to PTADOL after resting for 12 h at room temperature. For comparison, the precursor solvent for PDOL was prepared by dissolving 1.5M LiTFSI in 1 g DOL in an argon-filled glove box at room temperature. Then 8 mg TFB was added to the precursor solution and stirred until completely dissolved. The prepared solvents spontaneously converted to PDOL after resting for 12 h at room temperature.

Materials Characterization. ^{1}H NMR spectra were measured using a Bruker AVANCE II 400 spectrometer with dimethylsulfoxide-d6 (DMSO-d6) as solvent. The FTIR spectra (Bruker VERTEX 70, USA) of polymer samples were performed on an FT interferometer over a frequency range of 600–4000 cm^{-1}. The structure of each polymer was identified by XRD (D8 ADVANCE, Bruker) in the scanning range between 10°C and 60°C at a rate of 5° min^{-1}. The morphology of electrolyte membranes was characterized by AFM (Dimension Icon, Bruker), and field-emission scanning electron microscrope (SEM) (JEOL JSM-7610F Plus). ^{7}Li ssMAS NMR spectra of the polymers were measured by Bruker AVANCE III 400M spectrometer. The stress and strain curves of the samples were tested by a tensile testing apparatus (INSTRON 5965) at a stretching speed of 10 mm min^{-1} at room temperature. The thermal stability was obtained using a thermogravimetric analyzer (TGA 550, TA) under N_2 atmosphere with a heating rate of 10°C min^{-1} from 30 to 600°C. AXIS SUPRA + spectrometer was used to investigate the XPS of samples.

Electrochemical Measurements. The sandwich cells of SS (stainless steel)||SPEs||SS were used for the test of ionic conductivity by EIS experiments between 20°C and 80°C. Impedance data was obtained with an electrochemical working station VersaSTAT3 (USA) in the frequency range of 0.01–100 kHz with an AC amplitude of 5 mV. The ionic conductivity was calculated by using the following Eq. (1):

$$\sigma = \frac{L}{SR}$$

1

The electrochemical stability of PTADOL was obtained using the cell with Li/SHPE/stainless steel via linear sweep voltammetry (LSV). The voltage sweep was conducted at 0.1 mV s^{-1} from 1 to 5.5 V. The lithium ion transference number (t_{Li+}) was evaluated using a Li||PTADOL||Li cell. The cell was subjected to a polarization bias at 10 mV to determine the currents from the initial (I_0) to the steady state (I_s). The t_{Li+} was calculated according to the following Eq. (2):

$$t_{\mathrm{Li}^+} = \frac{I_{\mathrm{S}} R_{\mathrm{bulk}}(s)\left[\Delta V - I_0 R_{\mathrm{Li}}(0)\right]}{I_0 R_{\mathrm{bulk}}(0)\left[\Delta V - I_{\mathrm{S}} R_{\mathrm{Li}}(s)\right]}$$

2

where ΔV is the potential applied across the cell, $R_{bulk}(0)$, and $R_{bulk}(s)$ represent the initial and steady-state resistances of the SPEs, respectively. $R_{Li}(0)$ and $R_{Li}(s)$ are the initial and steady-state resistances of the passive layers on the lithium metal electrode.

Battery assembly. All batteries were assembled in an argon-filled glove box (H_2O < 0.1 ppm, O_2 < 0.1 ppm) and the *in-situ* formed polymer batteries were tested after 24 h of resting. The charging-discharging tests were performed on a Land battery testing system (Wuhan Land electronics Co. Ltd., China). LFP or NMC811 cathodes were prepared by mixing cathode material, carbon, polyvinylidene fluoride in N-Methyl-2-pyrrolidone with a weight ratio of 80:10:10. Then the homogenized slurry was cast on aluminum foil and dried in vacuum at 80°C overnight. The active material loading of the cathode is about 3.0 mg cm^{-2}.

In-situ DEMS test. The specially designed DEMS cell was assembled in an Ar filled glovebox. (O_2 and H_2O below 0.1 ppm, MBraun). The DEMS cell is made of 304 stainless steel. O-rings and fluorinated ethylene propylene films were put between the various parts of the battery for insulation. A poly tetra fluoroethylene sleeve was put into the cavity of the cell for insulation. NMC811 cathode, solid electrolyte, lithium metal, and perforated gasket were put into the cell in sequence. A spring with high stiffness coefficient was put between gasket and upper shell to make the cell impacted. The upper shell of the cell is directly connected to DEMS (HPR-40 DEMS, HIDEN ANALYTICAL).

Calculation Methods. *DFT calculations.* All quantum chemical calculations in this work were performed with B3LYP level using the framework of Gaussian 09 program package. The structure of PDOL and TTMAP were first optimized at the 6-31Gd level of theory by minimizing the energy without imposing molecular symmetry constraints based on Density Functional Theory (DFT). Single-point calculations were performed at the 6-311 + G(d,p) level of theory to calculate the binding energy, and the Lowest Unoccupied Molecular Orbital (LUMO) energy levels and the Highest Occupied Molecular Orbital (HOMO) energy levels could also be obtained, respectively. The binding energy (E_b) can be given as $E_b = E_{total} - (E_{polymer} + E_{Anion})$, where E_{total} is total energy of the system, $E_{polymer}$ is the energy of initial polymer, E_{Anion} is the energy of single anion (e.g. $TFSI^-$). The point charges on each atom were obtained by fitting the electrostatic potential surface with the RESP (Restrained Electro Static Potential) method using Multiwfn, and the local electronic function graph could be calculated.[43, 44]

Molecular dynamics simulations. Molecular dynamics (MD) simulations were performed to investigate the structures of SPEs. The classical MD simulations were carried out using GROMACS 2018.8[45] in this work. The Generalized Amber Force Field [46] was used along with Restrained ElectroStatic Potential charge generated by Multiwfn[44]. Initially, 30 PTADOL and 30 LiTFSI were packed using the packmol[47] software to simulate. For comparation, 40 PDOL and 30 LiTFSI were also packed. All the systems were

first heated from 0 K to 323 K in 100 ps, followed by 10 ns equilibration under the NPT (isothermal-isobaric ensemble) at 10 bar to equilibrate the electrolyte system. For the production run, an additional 50 ns NVT at 323 K (canonical ensemble) simulation was performed. At this state, all simulated systems were surely equilibrated. Visualization of the structures was achieved by VESTA software. To characterize the local structures surrounding Li^+ in the electrolyte, the radial distribution function was calculated using:

$$g(r) = \frac{1}{4\pi r^2 \rho} \frac{dn(r)}{dr}$$

3

where r is the distance of a species from the referenced Li^+, ρ is the average probability density of the Li^+ in the electrolyte, and dn(r) is the number of particles within a dr-thick spherical shell. By integrating the g(r) with respect to r, the CN of species surrounding the Li^+ center was obtained.

$$CN = 4\pi\rho \int_0^r r^2 g(r)\, dr$$

4

Declarations

Acknowledgement

This work is financially supported by the China Postdoctoral Science Foundation (No. 2022M711033), National Key Research and Development Program of China (2022YFE0202400) and National Natural Science Foundation of China (No. 22005085). The author would like to acknowledge the help from Prof. Xiaosheng Song at the Henan University at Kaifeng.

Author contributions

H. L. and C. G. L. designed this work. Y. F. D. performed the theoretical calculations. H. L. and L. Z. performed the experiments. H. L. analyzed the experimental results and wrote the manuscript. E. Q. Z. and W. D. Z. revised and finalized the manuscript.

Competing interests

The authors declare no competing interests.

Additional Information

Supplementary information The online version contains supplementary material available at ( ).

References

1. Hobold, G. M. et al. Moving beyond 99.9% Coulombic efficiency for lithium anodes in liquid electrolytes. Nat. Energy **6**, 951–960 (2021).
2. Yang, C. et al. Copper-coordinated cellulose ion conductors for solid-state batteries. Nature **598**, 590–596 (2021).
3. Chen, R., Li, Q., Yu, X., Chen, L. & Li, H. Approaching Practically Accessible Solid-State Batteries: Stability Issues Related to Solid Electrolytes and Interfaces. Chem. Rev. **120**, 6820–6877 (2019).
4. Fan, L.-Z., He, H. & Nan, C.-W. Tailoring inorganic-polymer composites for the mass production of solid-state batteries. Nat. Rev. Mater. **6**, 1003–1019 (2021).
5. Chen, X. R., Zhao, B. C., Yan, C. & Zhang, Q. Review on Li Deposition in Working Batteries: From Nucleation to Early Growth. Adv. Mater. **33**, 2004128 (2021).
6. Zhao, R. et al. Metal–organic frameworks for solid-state electrolytes. Energy & Environ. Sci. **13**, 2386–2403 (2020).
7. Zhou, Q., Ma, J., Dong, S., Li, X. & Cui, G. Intermolecular Chemistry in Solid Polymer Electrolytes for High-Energy-Density Lithium Batteries. Adv. Mater. **31**, 1902029 (2019).
8. Rosenwinkel, M. P., Andersson, R., Mindemark, J. & Schönhoff, M. Coordination Effects in Polymer Electrolytes: Fast Li^+ Transport by Weak Ion Binding. J. Phys. Chem. C **124**, 23588–23596 (2020).
9. Bocharova, V. & Sokolov, A. P. Perspectives for Polymer Electrolytes: A View from Fundamentals of Ionic Conductivity. Macromolecules **53**, 4141–4157 (2020).
10. Fenton, D. E., Parker, J. M. & Wright, P. Complexes of alkali metal ions with poly(ethylene oxide). Polymer **14**, 589 (1973).
11. Lu, J. et al. 4.2 V poly(ethylene oxide)-based all-solid-state lithium batteries with superior cycle and safety performance. Energy Storage Mater. **32**, 191–198 (2020).
12. Bae, J. et al. A 3D Nanostructured Hydrogel-Framework-Derived High-Performance Composite Polymer Lithium-Ion Electrolyte. Angew. Chem., Int. Ed. **57**, 2096 (2018).
13. Zhao, C. Z. et al. Rechargeable Lithium Metal Batteries with an In-Built Solid-State Polymer Electrolyte and a High Voltage/Loading Ni-Rich Layered Cathode. Adv. Mater. **32**, 1905629 (2020).
14. Liu, F. Q. et al. Upgrading traditional liquid electrolyte via in situ gelation for future lithium metal batteries. Sci. Adv. **4**, eaat5383 (2018).
15. Khan, K., Tu, Z., Zhao, Q., Zhao, C. & Archer, L. A. Synthesis and Properties of Poly-Ether/Ethylene Carbonate Electrolytes with High Oxidative Stability. Chem. Mater. **31**, 8466–8472 (2019).
16. Ma, Q. et al. Formulating the Electrolyte Towards High-Energy and Safe Rechargeable Lithium–Metal Batteries. Angew. Chem., Int. Ed. **60**, 16554 (2021).
17. Mackanic, D. G. et al. Crosslinked Poly(tetrahydrofuran) as a Loosely Coordinating Polymer Electrolyte. Adv. Energy Mater. **8**, 1800703 (2018).

18. Li, H., Du, Y., Zhang, Q., Zhao, Y. & Lian, F. A Single-Ion Conducting Network as Rationally Coordinating Polymer Electrolyte for Solid-State Li Metal Batteries. Adv. Energy Mater. **12**, 2103530 (2022).
19. Diederichsen, K. M., McShane, E. J. B. & McCloskey, D. Promising Routes to a High Li^+ Transference Number Electrolyte for Lithium Ion Batteries. ACS Energy Lett. **2**, 2563–2575 (2017).
20. Wen, S. et al. Integrated design of ultrathin crosslinked network polymer electrolytes for flexible and stable all-solid-state lithium batteries. Energy Storage Mater. **47**, 453–461 (2022).
21. Dong, T. et al. A multifunctional polymer electrolyte enables ultra-long cycle-life in a high-voltage lithium metal battery. Energy Environ. Sci. **11**, 1197–1203 (2018).
22. Chen, W. P. et al. Bridging Interparticle Li^+ Conduction in a Soft Ceramic Oxide Electrolyte. J. Am. Chem. Soc. **143**, 5717–5726 (2021).
23. Yao, Y. X. et al. Regulating Interfacial Chemistry in Lithium-Ion Batteries by a Weakly Solvating Electrolyte. Angew. Chem., Int. Ed. **60**, 4090 (2021).
24. Gadjourova, Z., Andreev, Y. G., Tunstall, D. P. & Bruce, P. G. Nature **412**, 520–523 (2021).
25. Lassègues, J. C., Grondin, & J. Talaga, D. Lithium solvation in bis(trifluoromethanesulfonyl)imide-based ionic liquids. Phys. Chem. Chem. Phys. **8**, 5629–5632 (2006).
26. Xu, B. et al. Interfacial Chemistry Enables Stable Cycling of All-Solid-State Li Metal Batteries at High Current Densities. J. Am. Chem. Soc. **143**, 6542–6550 (2021).
27. Kimura, K., Motomatsu, J. & Tominaga, Y. Correlation between Solvation Structure and Ion-Conductive Behavior of Concentrated Poly(ethylene carbonate)-Based Electrolytes. J. Phys. Chem. C **120**, 12385–12391 (2016).
28. Ebadi, M., Costa, L. T., Araujo, C. M. & Brandell, D. Modelling the Polymer Electrolyte/Li-Metal Interface by Molecular Dynamics simulations. Electrochim. Acta **234**, 43–51 (2017).
29. Yang, X. et al. Determining the limiting factor of the electrochemical stability window for PEO-based solid polymer electrolytes: main chain or terminal –OH group? Energy & Environ. Sci. **13**, 1318–1325 (2020).
30. Tominaga, Y. Kinno, & Y. Kimura, K. An end-capped poly(ethylene carbonate)-based concentrated electrolyte for stable cyclability of lithium battery. Electrochim. Acta **302**, 286–290 (2019).
31. Pandiana, S. et al. Electrochemical stability of ether based salt-in-polymer based electrolytes: Computational investigation of the effect of substitution and the type of salt. J. Power Sources **393**, 204–210 (2018).
32. Li, W. et al. SnF_2-Catalyzed Formation of Polymerized Dioxolane as Solid Electrolyte and its Thermal Decomposition Behavior. Angew. Chem., Int. Ed. **61**, e202114805 (2022).
33. Wang, Y. et al. A poly(1,3-dioxolane) based deep-eutectic polymer electrolyte for high performance ambient polymer lithium battery. Mater. Today Phys. **22**, 100620 (2022).
34. Wei, C. et al. Flexible and stable 3D lithium metal anodes based on self-standing MXene/COF frameworks for high-performance lithium-sulfur batteries. Nano Res. **14**, 3576–3584 (2021).

35. Li, T. et.al. Stable Anion-Derived Solid Electrolyte Interphase in Lithium Metal Batteries. Angew. Chem., Int. Ed., **133**, 22865 (2021).
36. Huang, Y. et al. Constructing Highly Conductive and Thermomechanical Stable Quasi-Solid Electrolytes by Self-Polymerization of Liquid Electrolytes within Porous Polyimide Nanofiber Films. Adv. Funct. Mater. **32**, 2201496 (2022).
37. Zhang, X. Q., Cheng, X. B., Chen, X., Yan, C. & Zhang, Q. Fluoroethylene Carbonate Additives to Render Uniform Li Deposits in Lithium Metal Batteries. Adv. Funct. Mater. **27**, 1605989 (2017).
38. Sun, F. et al. Self-Healable, Highly Stretchable, Ionic Conducting Polymers as Efficient Protecting Layers for Stable Lithium-Metal Electrodes. ACS Appl. Mater. Interfaces **14**, 26014–26023 (2022).
39. Shin, D. M. et al. A Single-Ion Conducting Borate Network Polymer as a Viable Quasi-Solid Electrolyte for Lithium Metal Batteries. Adv. Mater. **32**, 1905771 (2020).
40. Stolz, L. et al. Single-Ion versus Dual-Ion Conducting Electrolytes: The Relevance of Concentration Polarization in Solid-State Batteries. ACS Appl. Mater. Interfaces **14**, 11559 (2022).
41. Sun, H. et al. Fluorinated Poly-oxalate Electrolytes Stabilizing both Anode and Cathode Interfaces for All-Solid-State Li/NMC811 Batteries. Angew. Chem., Int. Ed. **60**, 18335 (2021).
42. Roesler, R. & Danielmeier, K. Tris-3-(1-aziridino)propionates and their use in formulated products. Prog. Org. Coat. **50**, 1–27 (2004).
43. Bayly, C. I., Cieplak, P., Cornell, W., & Kollman, P. A. A well-behaved electrostatic potential based method using charge restraints for deriving atomic charges: the RESP model. J. Phys. Chem. **97**, 10269–10280 (1993).
44. Lu, T., & Chen, F. Multiwfn: a multifunctional wavefunction analyzer. J. Comput. Chem. **33**, 580–592 (2012).
45. Abraham, M. J. et al. GROMACS: High performance molecular simulations through multi-level parallelism from laptops to supercomputers. SoftwareX **1**, 19–25 (2015).
46. Wang, J., Wolf, R. M., Caldwell, J. W., Kollman, P. A., & Case, D. A. Development and testing of a general amber force field. J. Comput. Chem. **25**, 1157–1174 (2004).
47. Martínez, L., Andrade, R., Birgin, E. G., & Martínez, J. M. PACKMOL: A package for building initial configurations for molecular dynamics simulations. J. Comput. Chem. **30**, 2157 (2009).

Figures

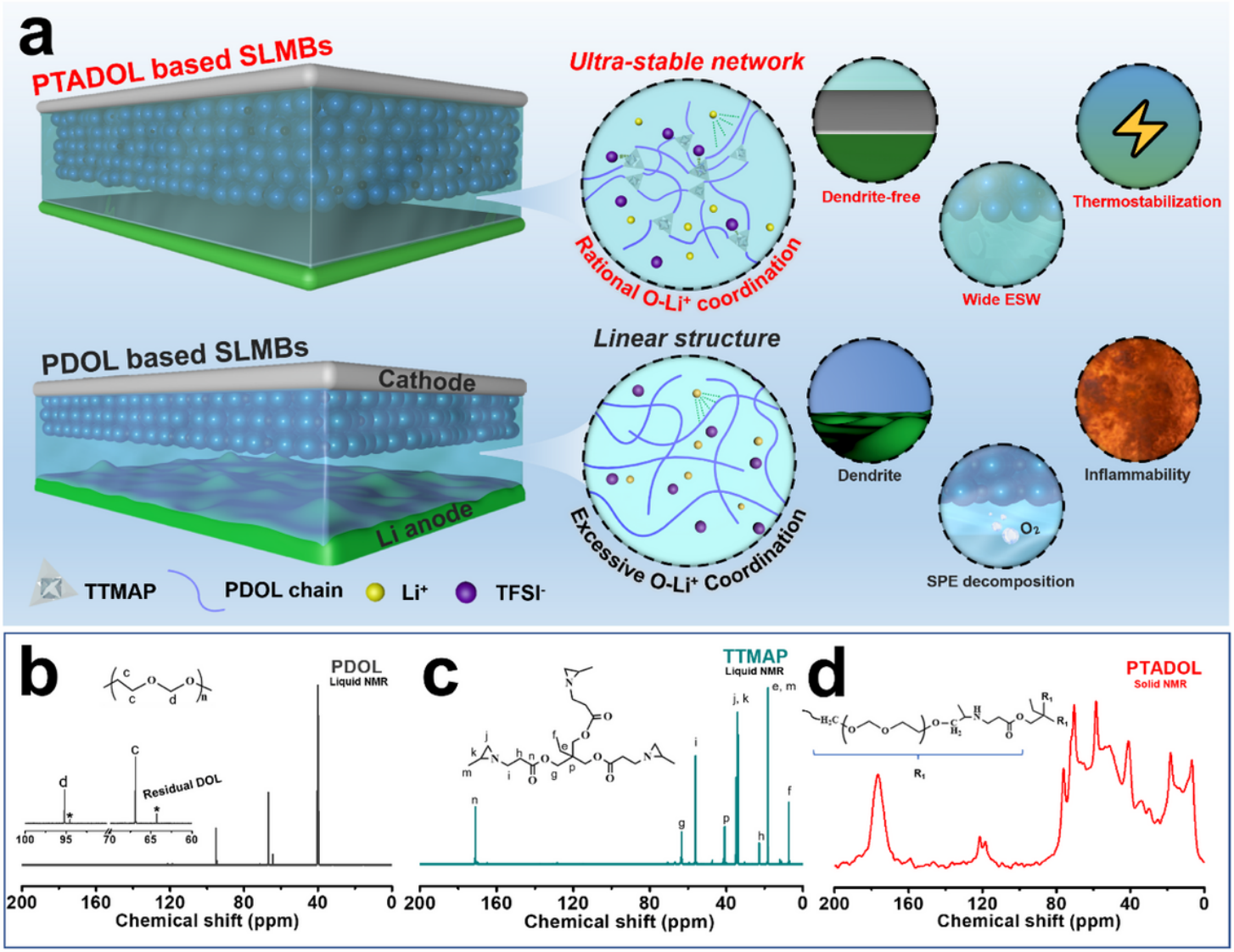

Figure 1

Mechanism and characterization of PTADOL. a Schematic diagram of PTADOL SPE with ultra-stable network structure and PDOL SPE with linear configuration. Liquid-state 13C NMR of **b** PDOL SPE and **c** TTMAP (DMSO-d6 as solvent). **d** Solid-state 13C NMR of PTADOL SPE.

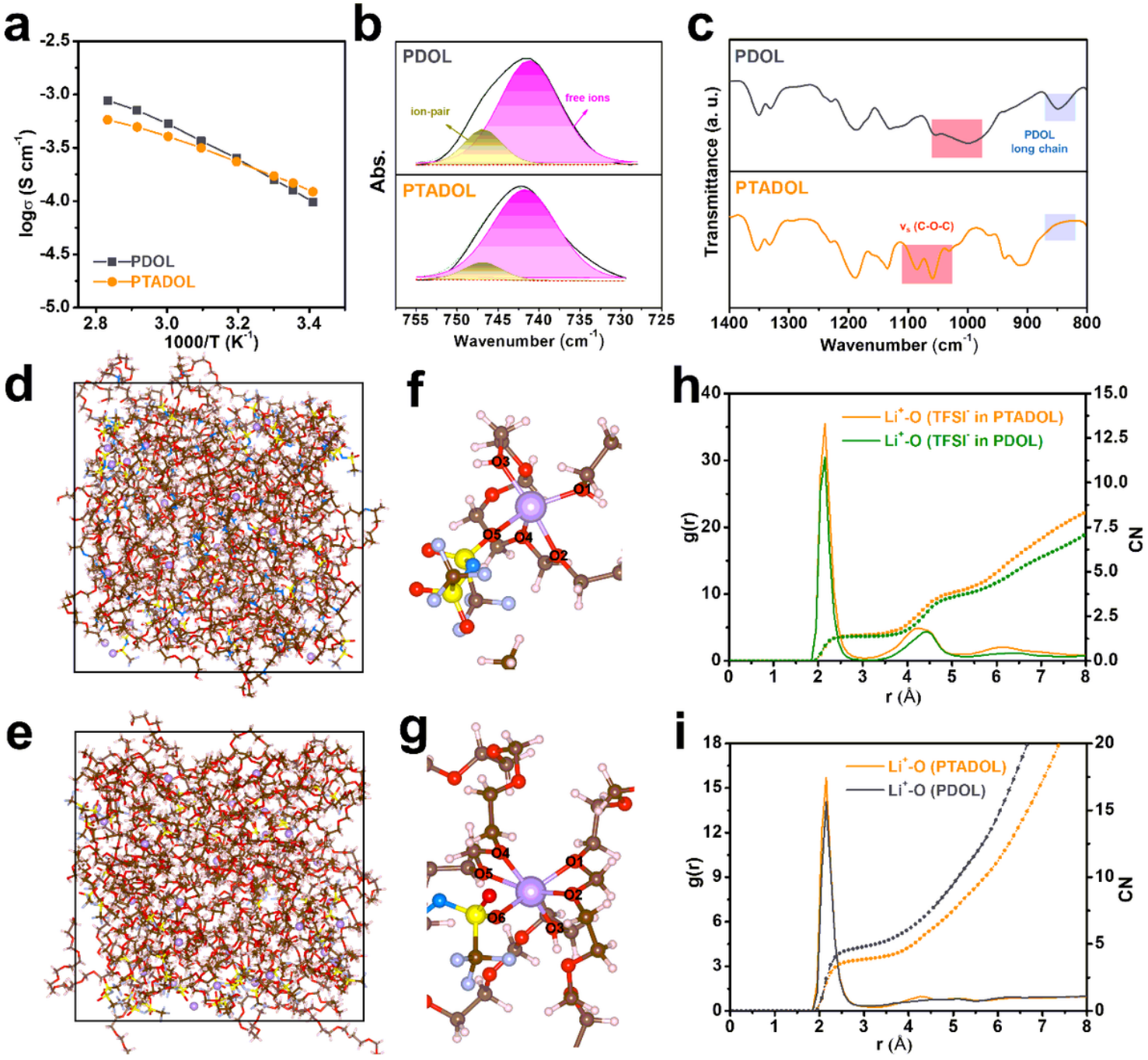

Figure 2

Chemistry analysis and theoretical calculation of PTADOL. a Temperature-dependent ionic conductivity of PTADOL and PDOL. **b, c** FTIR spectra of PTADOL and PDOL. Snapshots of PTADOL **d** and PDOL **e** obtained by MD simulation. The Li+and their first coordinated shells are presented by ball and stick model. Li+coordination structures of **f** PTADOL and **g** PDOL electrolytes. Calculated radial distribution functions (g(r), solid lines) and coordination numbers (CN, dash lines) for **h** lithium salt anions and **i** polymers.

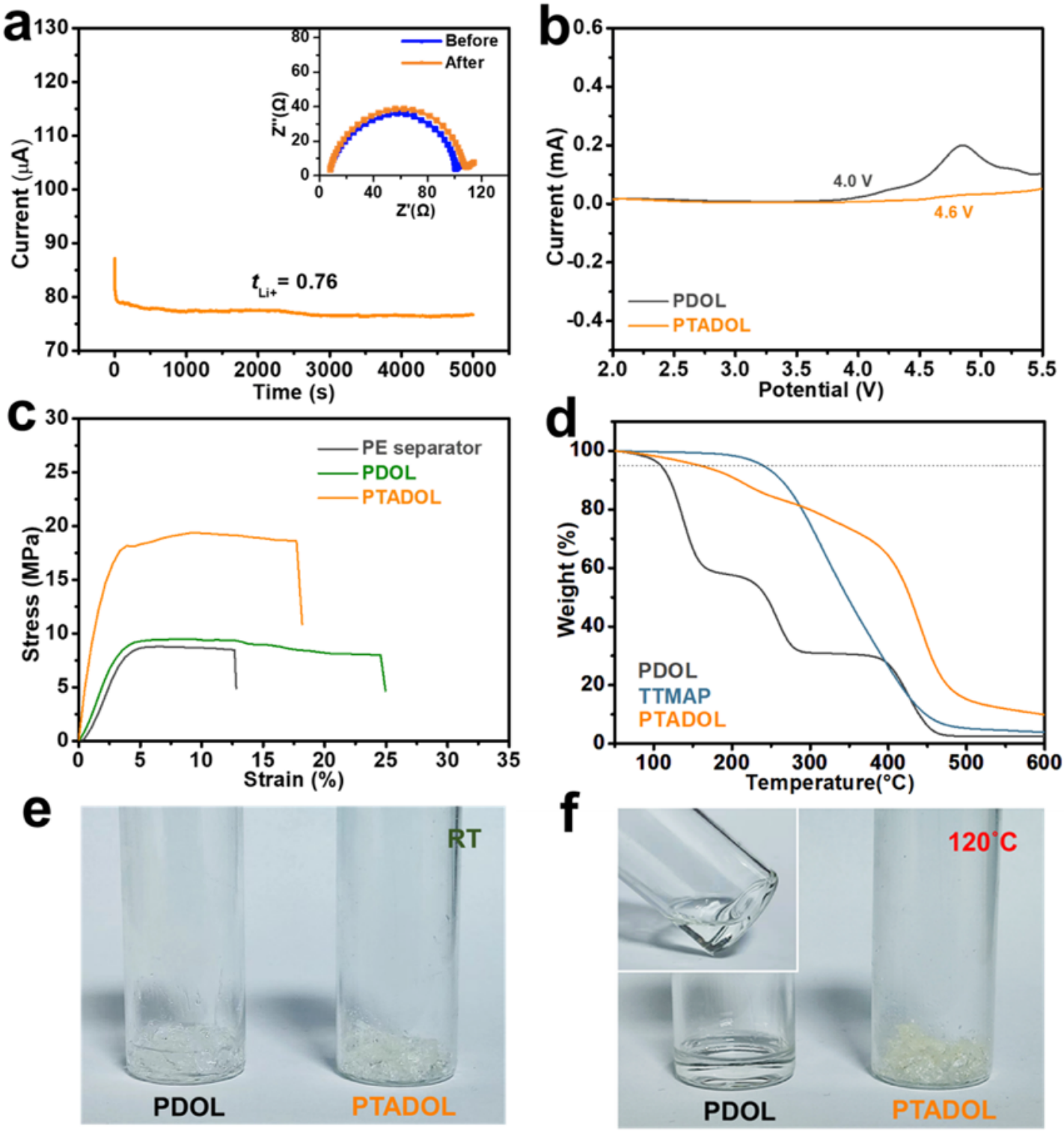

Figure 3

Electrochemical, mechanical and thermal stability of PTADOL. a Current-time profiles of the Li symmetrical cells with PTADOL. The inset shows the Nyquist impedance spectra of the batteries before and after polarization. **b** LSV curves of PTADOL and PDOL with a range of voltages from 2.0 to 5.5 V at room temperature. **c** Stress-strain plots of PTADOL, PDOL and PE separator. **d** TGA curves of PTADOL,

PDOL electrolytes, and TTMAP sample. The optic images of PTADOL and PDOL in glass tube **e** before and **f** after a heating treatment at 120°C for 20 mins.

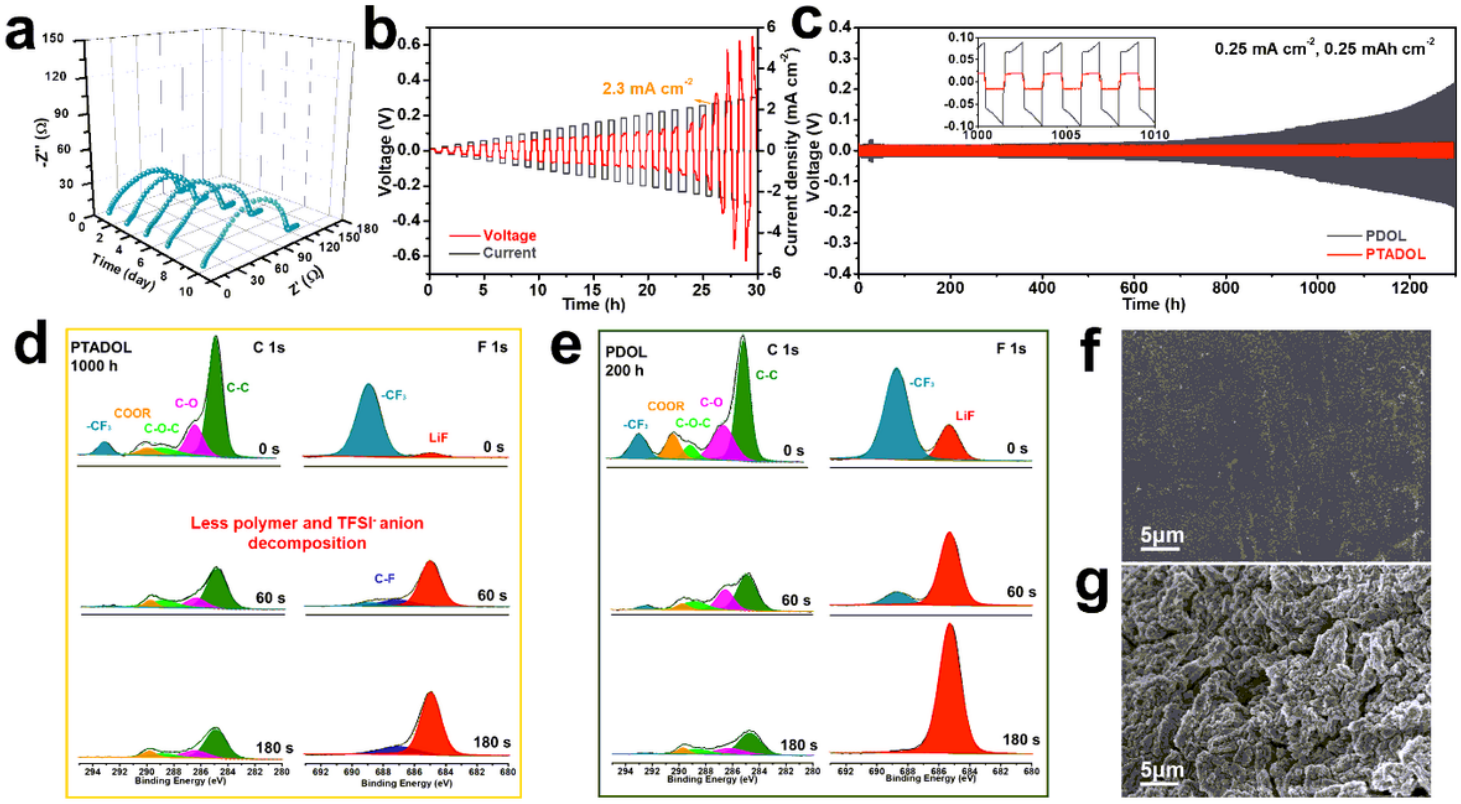

Figure 4

Electrochemical stability of PTADOL against lithium metal. a Impedance spectra for Li||PTADOL||Li batteries over different time. **b** Rate performance test of the Li|| PTADOL||Li battery to determine its CCD. **c** Voltage profiles of the Li||PTADOL||Li and Li||PDOL||Li symmetric batteries at a current of 0.25 mA cm−2and at 30 °C. Insets: Detailed voltage profiles of the 1000 - 1010 h. XPS spectra of C 1s and F1s of the cycled lithium metal in **d** Li||PTADOL||Li and **e**Li||PDOL||Li symmetric batteries. SEM images of lithium metal after Li plating/stripping 1200 h in **f** Li||PTADOL||Li battery and **g** Li||PDOL||Li battery.

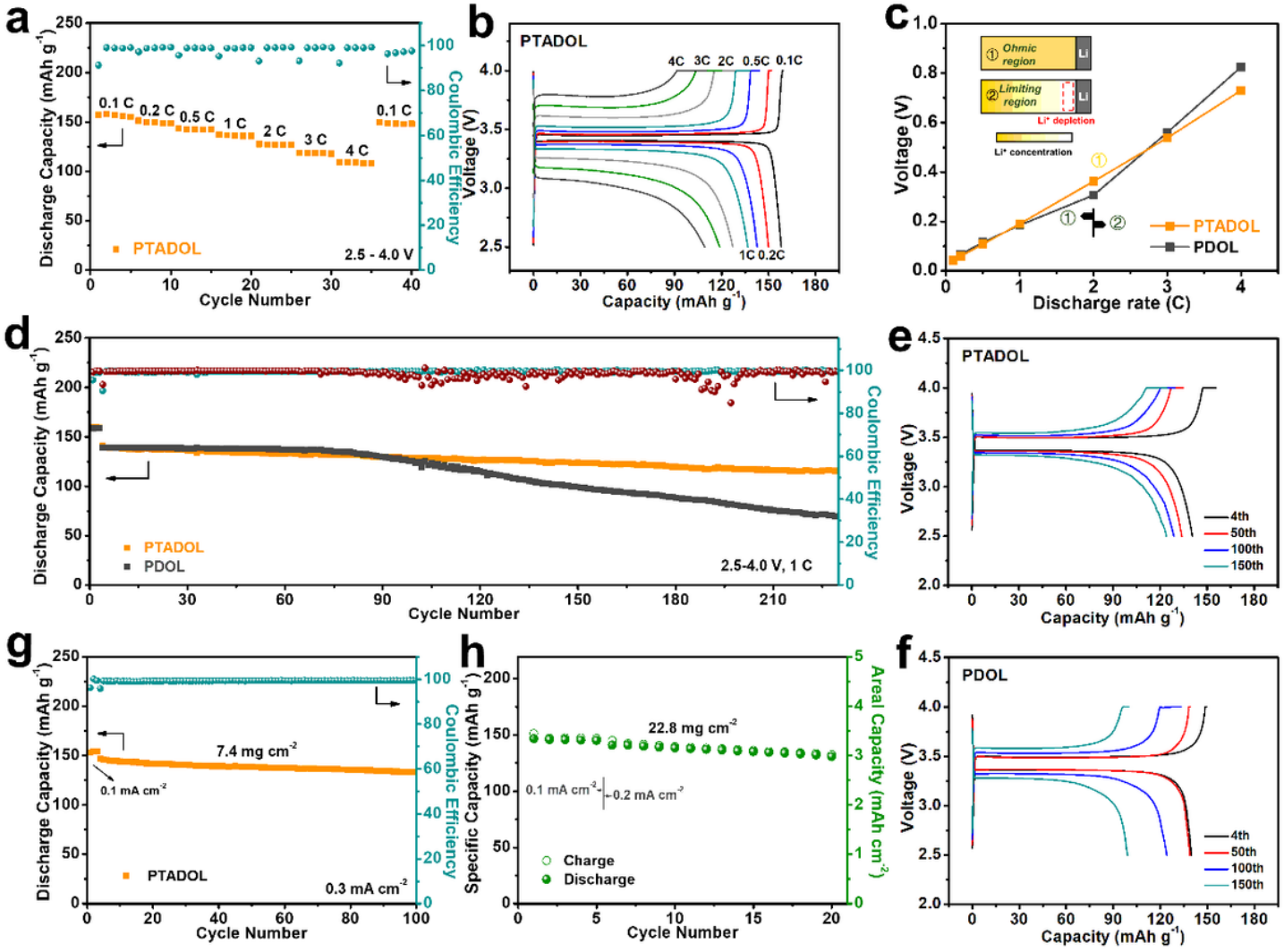

Figure 5

Electrochemical performance of SLMBs with LFP cathode. a Rate capability, and **b** charge-discharge voltage profiles of LFP||PTADOL||Li battery at various rates. **c** Overpotential of LFP||PTADOL||Li and LFP||PDOL||Li batteries at various rates. **d** Capacity retention performance of PTADOL and PDOL based batteries at 2.5-4.0 V and 1 C.Typical charge-discharge voltage profiles of **e** LFP||PTADOL||Li battery and **f**LFP||PDOL||Li battery; Cycling performance of PTADOL based batteries with **g** 7.4 mg cm−2 **h** 22.8 mg cm−2 LFP loading.

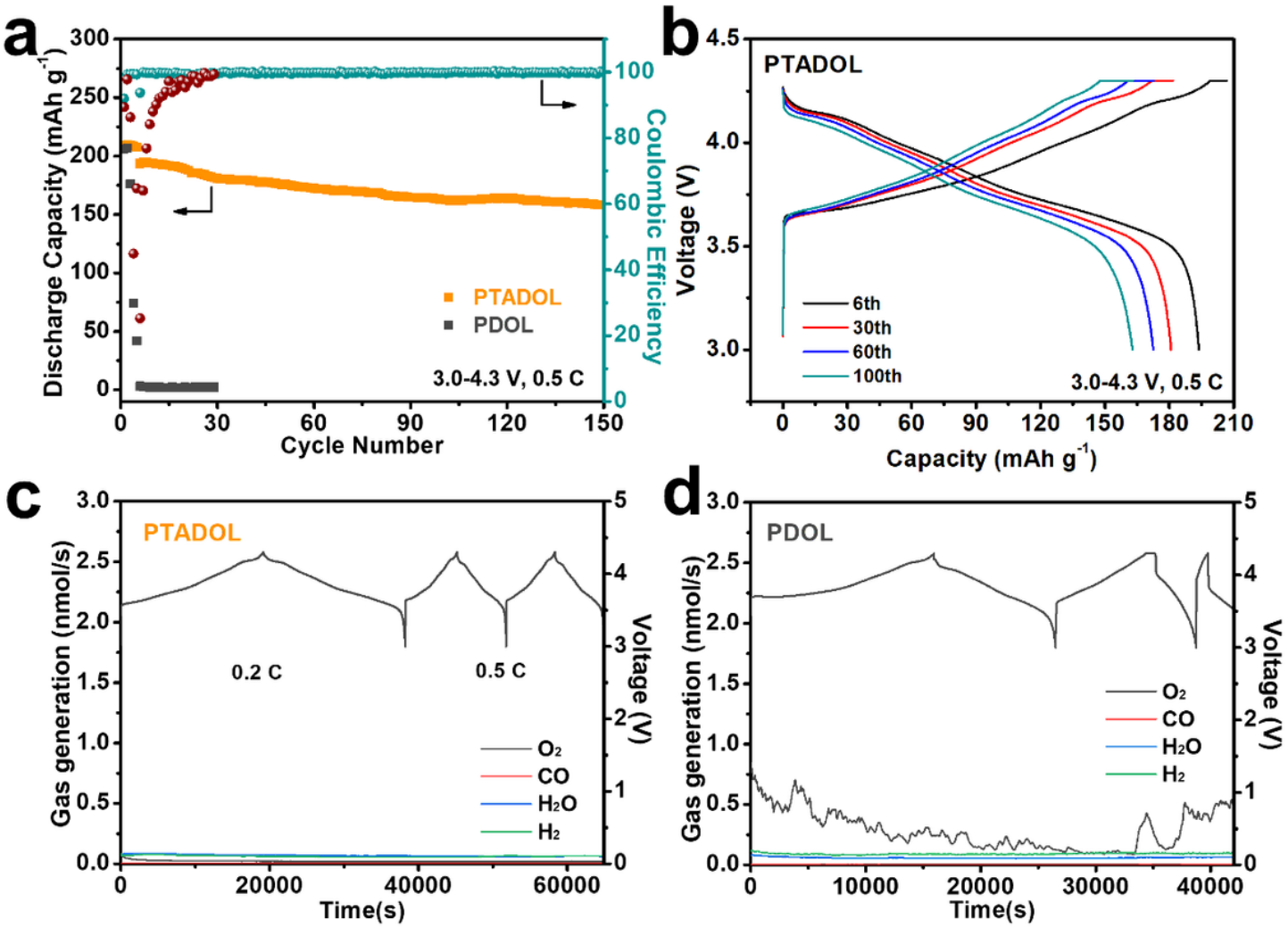

Figure 6

Electrochemical performance and decomposition behavior of SLMBs with NMC cathode. (a) Cycling performance of the batteries at 3.0-4.3 V and 0.5 C. (b) Typical charge-discharge voltage profiles of the PTADOL based batteries. *In-situ*DEMS results of mass signals *m/z* 2 (H2), 18 (H2O), 28 (CO), and 32 (O2) of NMC811||Li batteries with (c) PTADOL and (d) PDOL and corresponding voltage profiles.

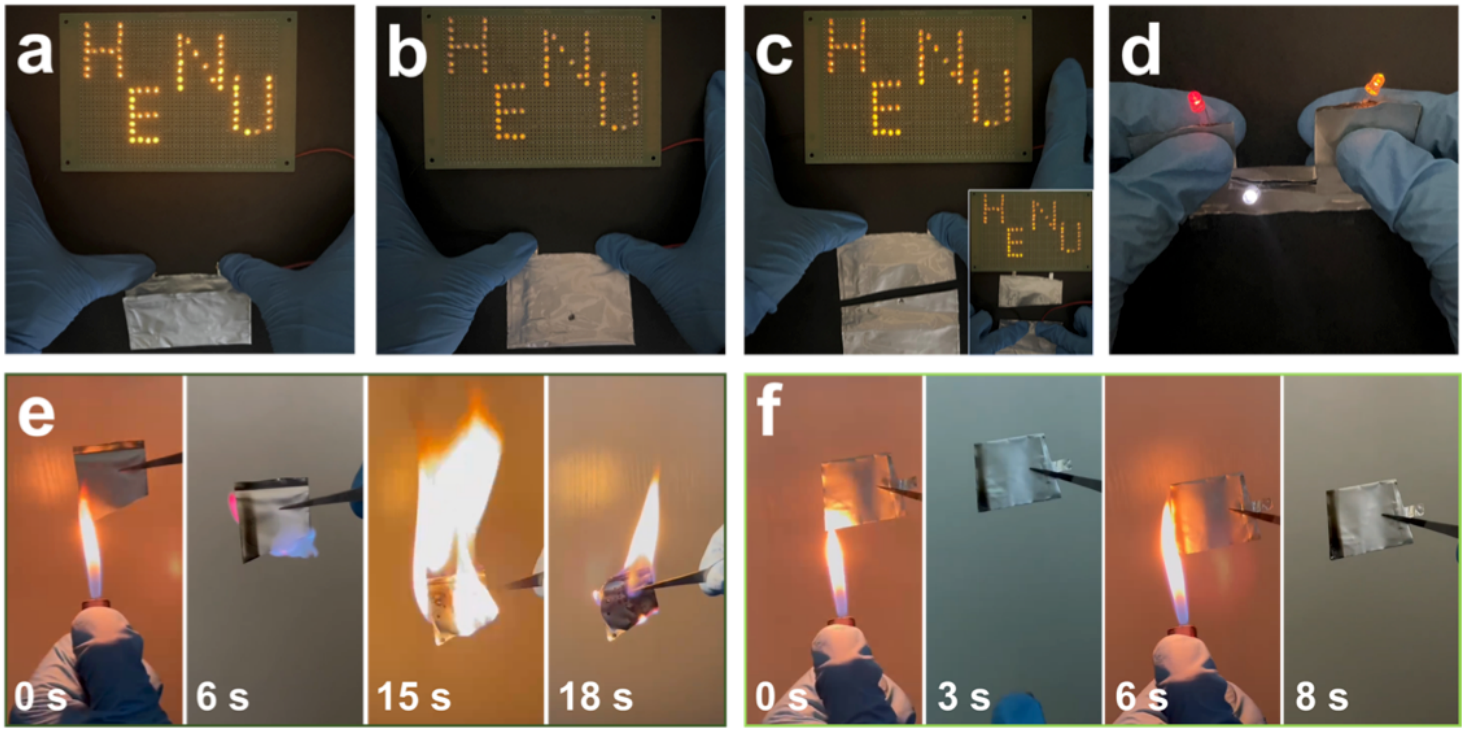

Figure 7

Safety characterization of PATDOL based solid-state pouch cells. Photographs of NMC811||PTADOL||Li pouch cell lighting LED array after (a) being bent, (b) needle penetrated, and (c-d) cut in pieces. Flame test of the (e) NMC811||PDOL||Li, and (f) NMC811||PTADOL||Li pouch cell.

Supplementary Files

This is a list of supplementary files associated with this preprint. Click to download.

- SupportingInformationPTADOL0825.docx
- Tableofcontents.docx
- VideoS1PTADOL.mp4
- VideoS2PDOL.mp4